PHILIPPINE ENGINEERING JOURNAL
PEJ 2022; Vol. 43, No. 2: 23-42

Received: 06 July 2022
Accepted: 23 October 2022

Electrochemical Corrosion of as-cast Pb-Ca-Sn Grid in Simulated Battery Electrolytes

Jan Lowell P. Buquiz and Manolo G. Mena
Department of Mining, Metallurgical, and Materials Engineering
University of the Philippines Diliman Quezon City, Philippines

Abstract *– Pb-Ca-Sn alloys are one of the primary materials for the positive grids of automotive batteries. Despite the various developments in the properties of such alloys, positive grid corrosion remains to be one of the leading causes of battery failure. The study aims to determine the corrosion behavior of various parts of an as-cast Pb-Ca-Sn alloy used in service to provide insights on improving grid design and casting conditions. Experiments were carried out using Pb-Ca-Sn grids taken from the production line of a battery manufacturing plant. Two grid locations, A and B, were used to compare the difference in cooling rates during manufacturing. The chemical composition and microstructure of each grid location were characterized. Electrochemical Impedance Spectroscopy (EIS) plots, equivalent circuit analysis, and potentiodynamic polarization curves were used to evaluate electrochemical behavior at various test conditions. Chemical analysis showed that the composition of each grid location is similar. Photomicrographs illustrated that the microstructures are characterized by cellular structures consisting of the Pb-rich α phase with eutectic mixtures on the intercellular boundaries. Moreover, grain and cellular sizes are larger in A than in B. EIS results showed that the R_{CT} decreased as the working temperature increased. The decrease in R_{CT} may be associated with the reduction of active porous sites due to the formation of a more compact $PbSO_4$ layer. On the other hand, the R_P increased as the acid concentration and temperature increased for both grid locations. Furthermore, the R_P values at B are higher than in A. R_P increase may also be associated with the formation of a thicker passivating corrosion layer, suggesting faster corrosion rates at location B. The higher corrosion rates in B may be attributed to its finer grain size and cellular size. Polarization curves also showed that the R_P increased with temperature increase.*

Keywords: corrosion, EIS, lead-acid batteries, lead alloys, microstructure

I. INTRODUCTION

Corrosion of the positive grid remains to be one of the leading causes of battery failure. Several alloys, such as lead-antimony (Pb-Sb) and lead-calcium (Pb-Ca), have been investigated to be suitable materials for the positive grids of automotive batteries. Pb-Sb alloys are used for their excellent mechanical properties and castability. However, corrosion rates are relatively high in Pb-Sb alloys. The antimony is also released during the corrosion process and lowers the hydrogen overvoltage of the negative grid, resulting in rapid self-discharge and water loss. On the other hand, Pb-Ca alloys have lower self-discharge rates and water losses in service, making them suitable for maintenance-free batteries. The Pb-Ca alloys also have higher corrosion resistance than Pb-Sb alloys [1–4].

The use of Pb-Ca alloys has its drawbacks. Pb-Ca alloys have lower yield strength and tensile strength than Pb-Sb alloys. It forms a passivating layer with high impedance, increasing the difficulty of recharging the battery. Other alloying elements, such as aluminum, silver, and tin, are introduced to address these issues.

Adding Sn to Pb-Ca alloys improves the mechanical and electrochemical properties [2,3]. In Pb-Ca-Sn alloys at an Sn/Ca ratio of at least 12:1, all of the Ca precipitates as Sn_3Ca instead of Pb_3Ca [1,5]. Sn_3Ca strengthens the alloy more than Pb_3Ca [2,6]. The strengthening is associated with the larger misfit of the smaller continuous Sn_3Ca precipitates in the lead lattice than the coarser discontinuous Pb_3Ca precipitates. Despite the developments in lead-acid battery components for automotive applications, corrosion of the positive grids is a significant problem [1].

The cellular microstructure of as-cast grids influences the surface corrosion of Pb alloys. The microstructure depends on the solidification rates during grid casting, so not all locations will experience the same rate [7,8]. The difference in cooling rates results in varying microstructures leading to different corrosion tendencies. Determining the corrosion behavior of various locations in an as-cast grid will give insights into improving grid design and casting conditions. The objective of the study is to determine the corrosion behavior of the different locations of as-cast Pb-Ca-Sn alloy at various acid concentrations and working temperatures.

II. METHODOLOGY

Experiments were carried out using as-cast Pb alloys taken from one of the production lines of a battery manufacturing plant. Two different grid locations were used in this study, as shown in Figure 1. The locations were chosen to compare the difference in cooling rates during manufacturing. Location A was adjacent to a hotspot and was expected to have relatively slower cooling rates than Location B, which was in contact with a metal ejector pin that pushed the grid out of the mold.

Before conducting the electrochemical tests, each grid location was characterized. The chemical composition of each grid location was determined using an X-Ray Fluorescence Spectrometer (XRF) and an Inductively Coupled Plasma – Optical Emission Spectroscopy (ICP-OES). The Pb, Sn, and other elements were quantified using XRF, while the Ca content was determined through ICP-OES. The microstructure was characterized through Optical Microscopy. The metal samples were mounted using a fast gel premix polyester resin for easy handling. The mounted samples were then subjected to metallographic preparation. Grinding was manually done using silicon carbide abrasive papers up to 1200 grit finish. Mechanical polishing was done against a rotating cloth using a one-micron alumina suspension. The samples were etched by immersion in a solution of three-parts glacial acetic acid and one-part hydrogen peroxide (30%) for three to five seconds. Photomicrographs were taken using ZEISS Primotech Light Microscope under brightfield illumination.

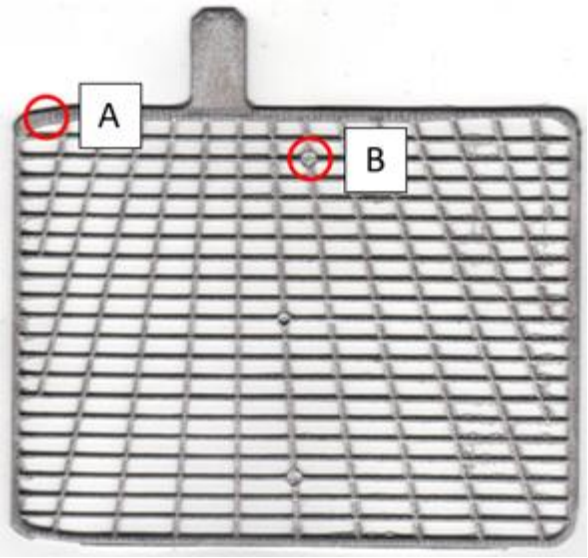

Figure 1. Locations of interest in the grid samples (A and B)

The electrochemical tests were carried out using a three-electrode cell setup. The working electrode was produced by soldering the back of the metal sample to a copper wire. The wire was then inserted into a six-mm diameter glass tube. The sides and soldered portion were covered with an acid-resistant epoxy resin, ensuring that only the front surface would be exposed to the electrolyte during the electrochemical tests. The exposed surface was ground and polished to remove the oxide layer produced after casting. Manual grinding was done using silicon carbide abrasive papers up to 1500 grit finish. Mechanical polishing was done against a rotating cloth using a one-micron alumina suspension. The working electrode was then washed with deionized water and dried with ethanol.

The fabricated working electrode and the platinum sheet counter electrode were immersed in a 60 mL sulfuric acid electrolyte. On the other hand, the mercury/mercurous sulfate reference electrode (MSE) was immersed in a 60 mL saturated (2 M) potassium sulfate solution. A Luggin capillary connected the working electrode with the reference electrode. The H_2SO_4 electrolyte was prepared using analytical grade stock solution and deionized water. The saturated (2 M) potassium sulfate was prepared using analytical grade potassium sulfate in deionized water. Fresh solutions were used for each experimental run and electrochemical test.

The electrochemical tests were conducted at various operating conditions, as indicated in Table 1. The levels for each factor were chosen to simulate battery conditions. The H_2SO_4 concentrations used were comparable to concentrations used in actual batteries. The temperatures 28℃ and 40℃ corresponded to room temperature storage and in-service battery conditions, respectively. For experiments at 40℃, the three-electrode setup was immersed in a temperature-controlled water bath.

Table 1. Test Parameters Used

Variables	Factor Levels
Location	A
	B
H_2SO_4 Concentration (%V/V)	15
	25
Temperature (°C)	28
	40

Before any electrochemical test, a pretreatment procedure was employed to remove any oxide formed during the sample preparation. The pretreatment was done by applying -1.0 V (MSE) versus the open-circuit potential (OCP) for 5 minutes. The OCP used was the measured average value after 10 minutes or when dE/dt was less than 1 μV/s. The Electrochemical Impedance Spectroscopy was carried out at OCP. The potential amplitude was set to 10 mV with 10 points per decade. The AC impedance was measured from 100 kHz to 100 mHz. After EIS, Potentiodynamic polarization was conducted by scanning the potential at a range of -250 mV (MSE) to +250 mV (MSE) versus OCP. The scanning rate was set at 0.15 mV/s to minimize the effect on the current produced at the different potentials.

III. RESULTS AND DISCUSSION

3.1 Sample Characterization

The composition for each grid location is listed in Table 2. Results show that the chemical composition of each grid location is comparable with each other.

Table 2. Chemical composition of each grid location (% weight)

Grid Location	Element			
	Pb	Ca	Sn	Other
A	97.85	0.07	1.40	Bal
B	97.86	0.07	1.38	Bal

The photomicrographs at different grid locations are shown in Figures 2 and 3. The as-cast microstructures are defined by large grains greater than 100 microns with a cellular substructure [2]. The cellular structures consist of the Pb-rich α phase with eutectic mixtures on the intercellular boundaries [9,10]. In general, the grain size and cellular arrays of location A are greater than that of B. On the other hand, the grains are more elongated in location B. The larger grains and cellular structures of location A indicate a slower cooling rate than B.

Figure 2. Photomicrograph of Location A at 100x magnification

Figure 3. Photomicrograph of Location B at 100x magnification

3.2 Electrochemical Impedance Spectroscopy Measurements

Representative Bode modulus (Z vs. log f) and Bode phase (θ vs. log f) plots, along with replicate plots obtained at different electrolyte concentrations for each grid location at ambient temperature, are shown in Figures 4 and 5. The impedance responses at high frequencies, 10^5 – 10^4 Hz, are associated with the solution resistance (R_{sol}) [11]. The phase shift angle for a resistive element is 0° [12]. However, it can be seen from Figures 4 and 5 that the minimum phase shift angle from all the samples at the high frequency range is 35°. The deviation may have resulted from instrumental errors. Electrical cables and alligator clips may induce stray capacitance at high frequencies [11,13]. The impedance responses between 10^4 – 10^3 Hz depict the maximum phase shift angle occurrence for all test conditions. However, the maximum

phase shift angles are not equal to 90° indicating a non-ideal capacitive behavior [12]. The capacitance can be associated with the formation of an electrical double layer, while the non-ideal behavior may be attributed to surface defects and roughness [7,11,14]. On the other hand, the impedance responses at low frequencies illustrate phase shift angles greater than zero. The non-zero phase shift angles at the lowest frequency (0.1 Hz) indicate that the electrode behavior is not purely resistive.

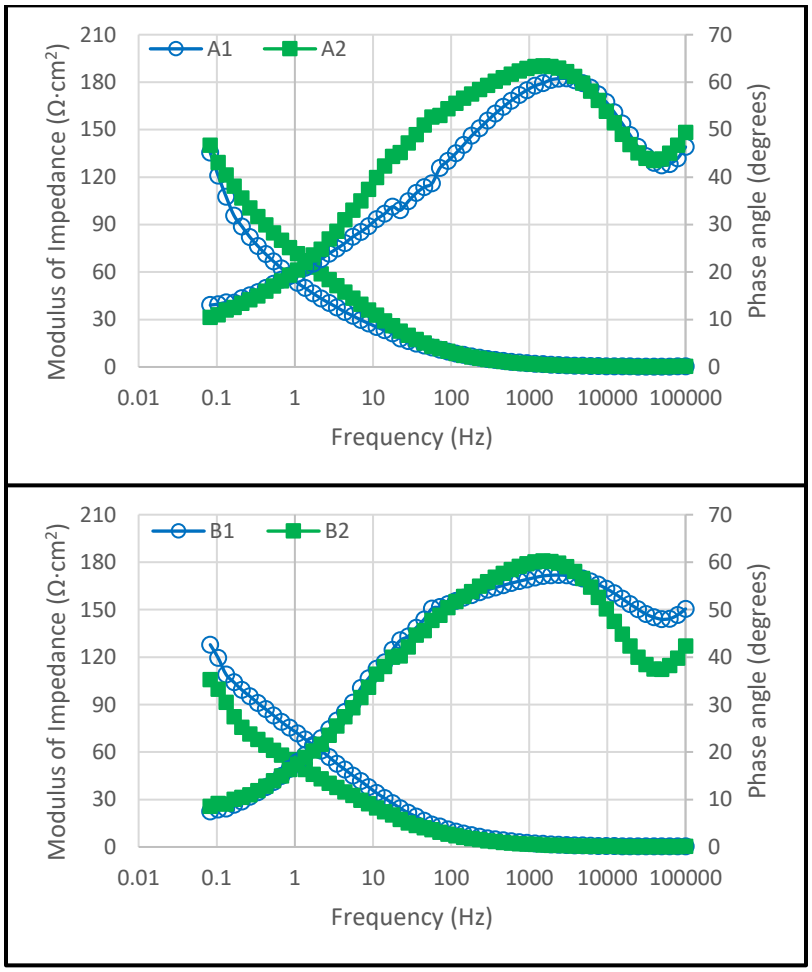

Figure 4. Bode plots for Location A (top) and Location B (bottom) at 15% (V/V) H_2SO_4 at 28°C

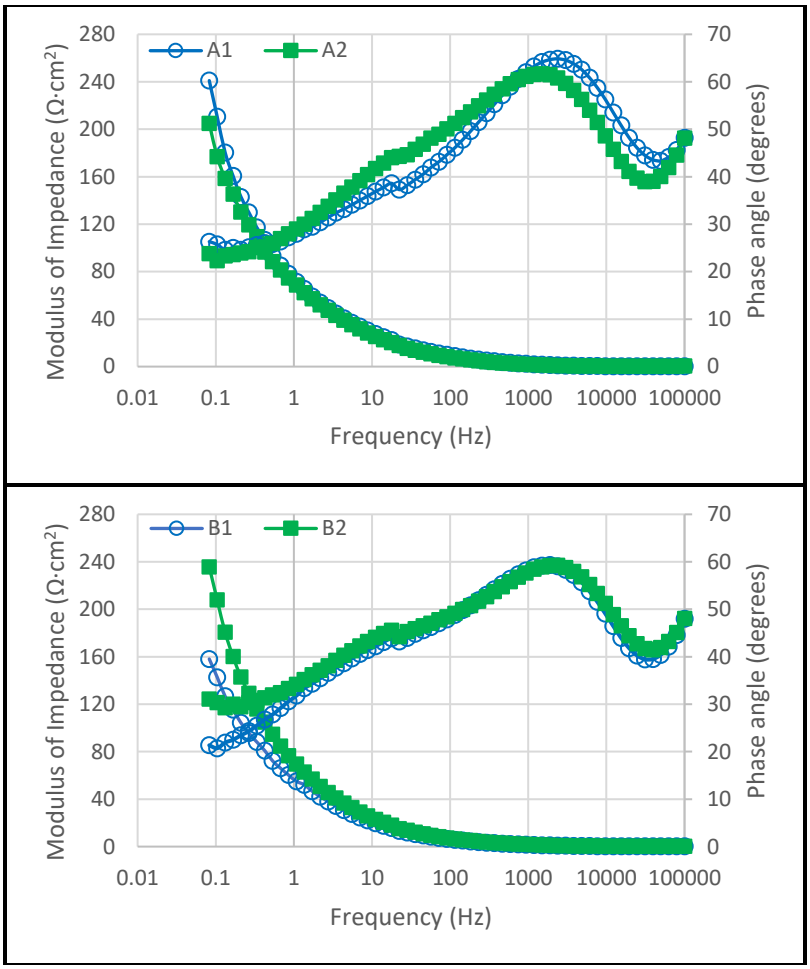

Figure 5. Bode plots for Location A (top) and Location B (bottom) at 25% (V/V) H_2SO_4 at 28°C

Representative Bode modulus (Z vs. log f) and Bode phase (θ vs. log f) plots, along with replicate plots, obtained at different electrolyte concentrations for each grid location at 40°C, are shown in Figures 6 and 7. Some observations at ambient temperature can also be seen at 40°C. The minimum phase shift angles at high frequencies are also greater than zero. The R_{sol} values are minimal for both temperatures, showing that the solutions have high ionic conductivity. The electrode also behaves as a non-ideal resistor, as indicated by the non-zero phase shift angles at 0.1 Hz. The non-ideal capacitive behavior of the electrical double layer can also be observed, as shown by the maximum angles of less than 90°.

On the other hand, the frequency domain in which the maximum phase shift angle occurs is shifted from 10^4 - 10^3 to 10^2 - 10^1 Hz. The system also becomes slightly unstable at the 10^2 - 10^1 Hz domain. The instability may be caused by reactions occurring at the working electrode. $PbSO_4$ is formed when Pb is immersed in H_2SO_4. However, $PbSO_4$ is also soluble in H_2SO_4 [15,16]. The increase in temperature may have affected the formation and dissolution rates of $PbSO_4$. The simultaneous formation and dissolution of $PbSO_4$ may have disturbed the electrical double layer, resulting in instability during measurements.

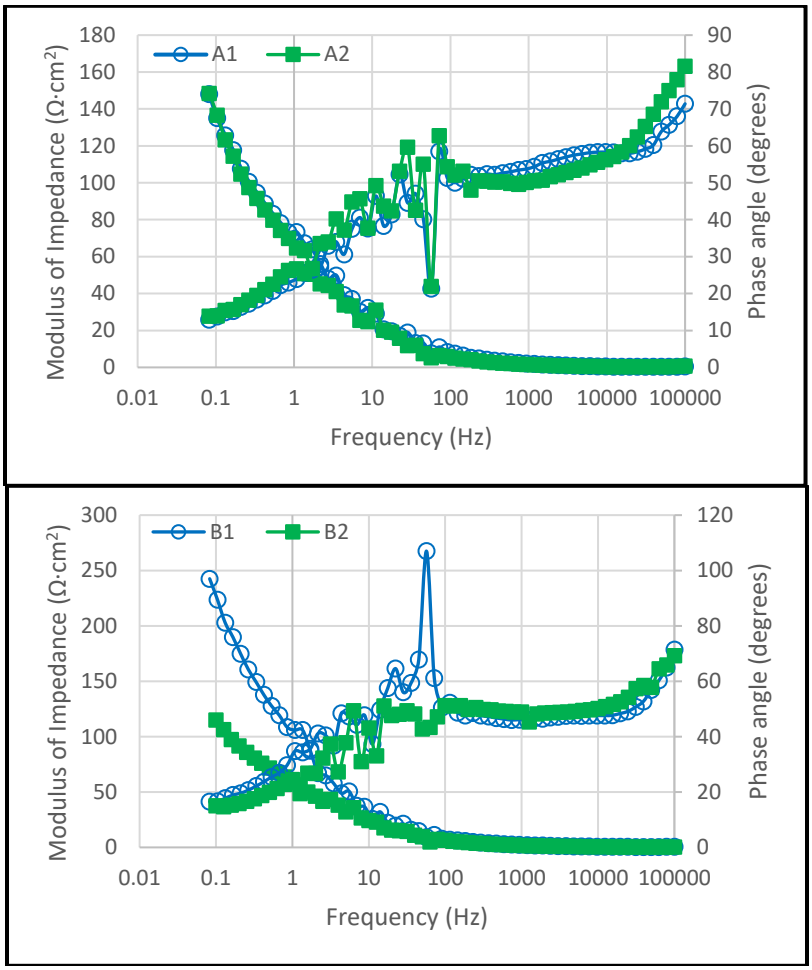

Figure 6. Bode plots for Location A (top) and Location B (bottom) at 15% (V/V) H_2SO_4 at 40°C

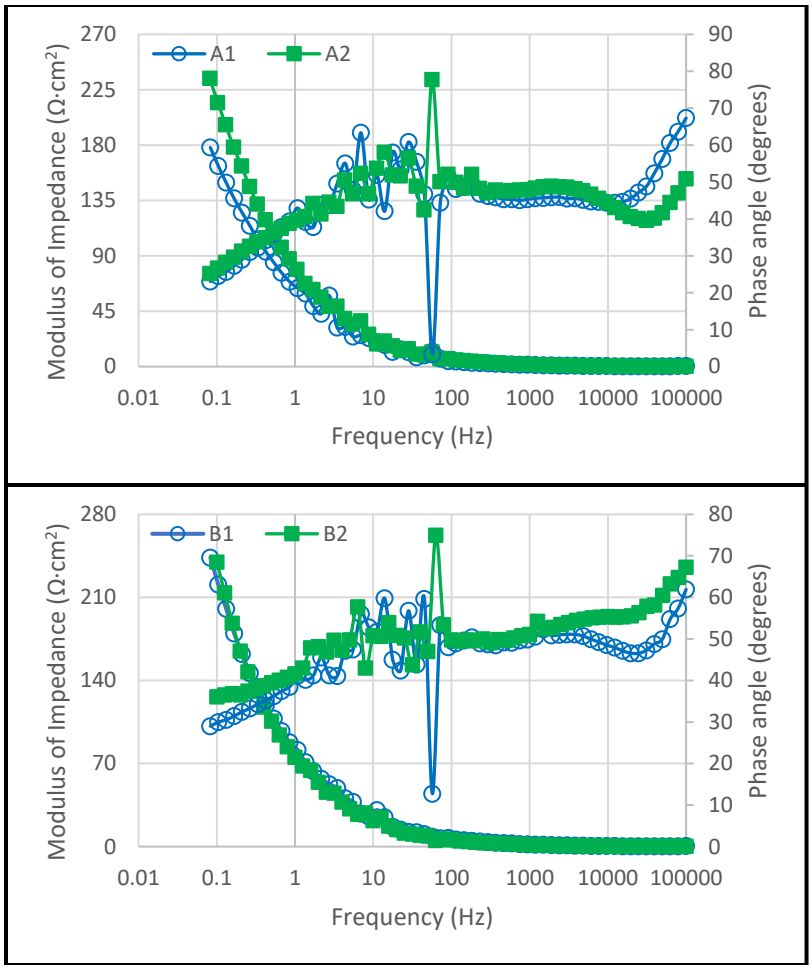

Figure 7. Bode plots for Location A (top) and Location B (bottom) at 25% (V/V) H_2SO_4 at 40°C

Representative Nyquist plots and replicate plots for each acid concentration at 28°C are shown in Figures 8 and 9, while plots at 40°C are illustrated in Figures 10 and 11. The Nyquist plots are characterized by the presence of a depressed capacitive loop at high frequencies (10^5 – 10^0), similar to the findings of Osorio et al. [10,17]. For both temperatures, the diameter of the capacitive arcs increased when the acid concentration was increased from 15% to 25%, indicating higher impedances at higher acid concentrations. On the other hand, the shape and size of the capacitive arcs for each grid location are comparable.

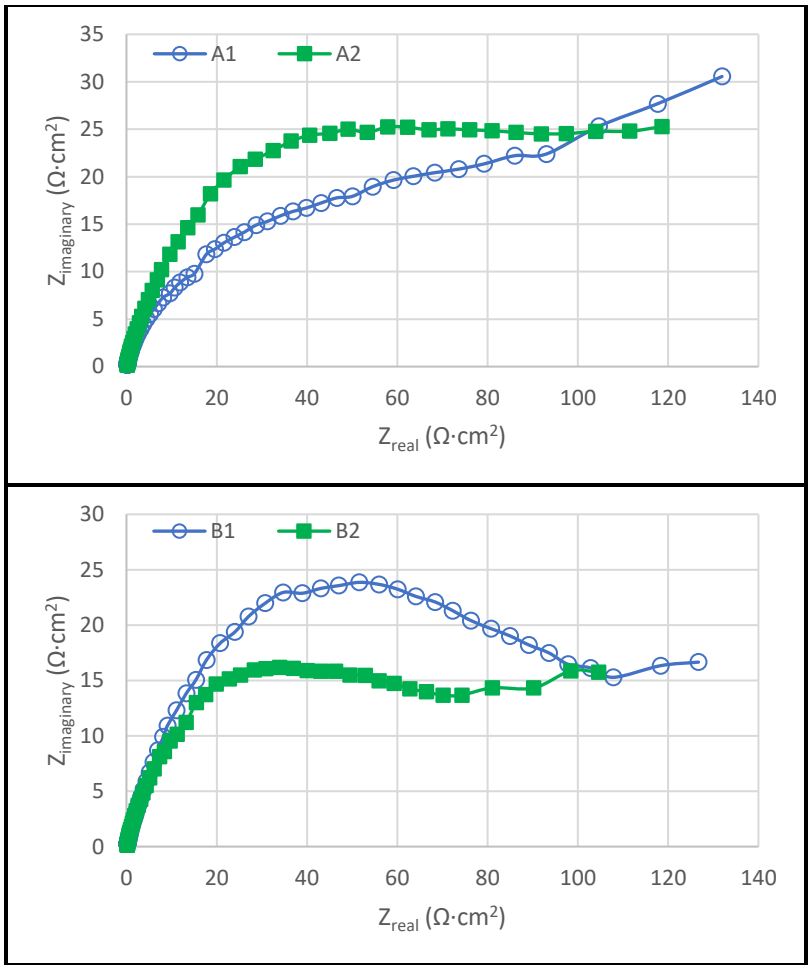

Figure 8. Nyquist plots for Location A (top) and Location B (bottom) at 15% (V/V) H_2SO_4 at 28°C

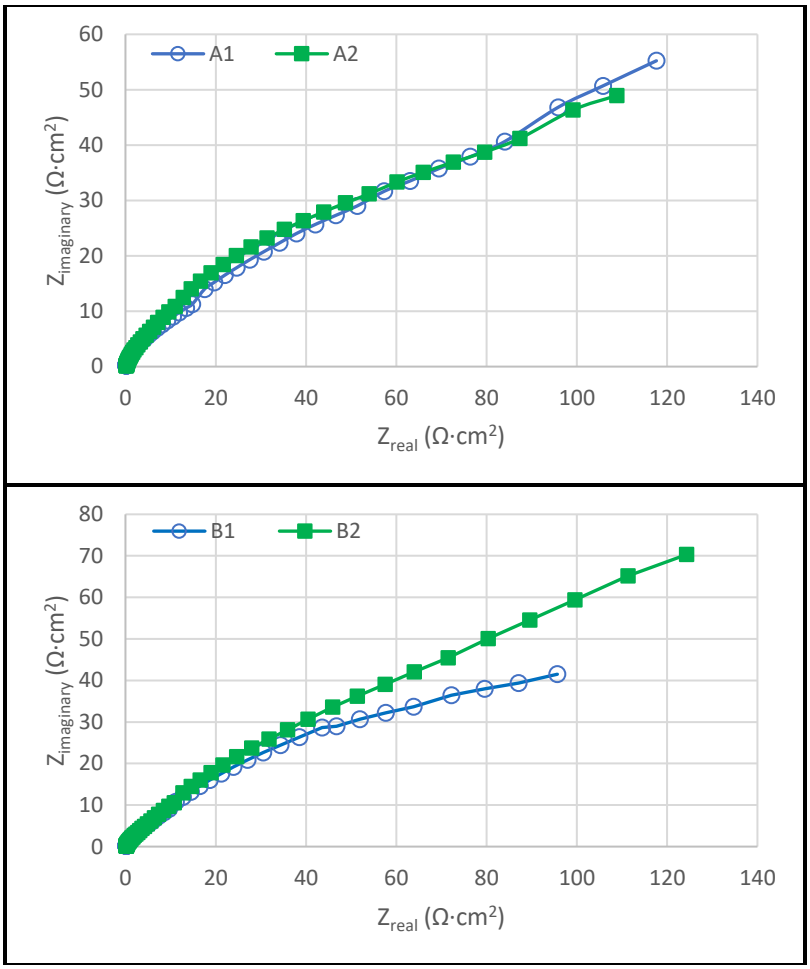

Figure 9. Nyquist plots for Location A (top) and Location B (bottom) at 25% (V/V) H_2SO_4 at 28°C

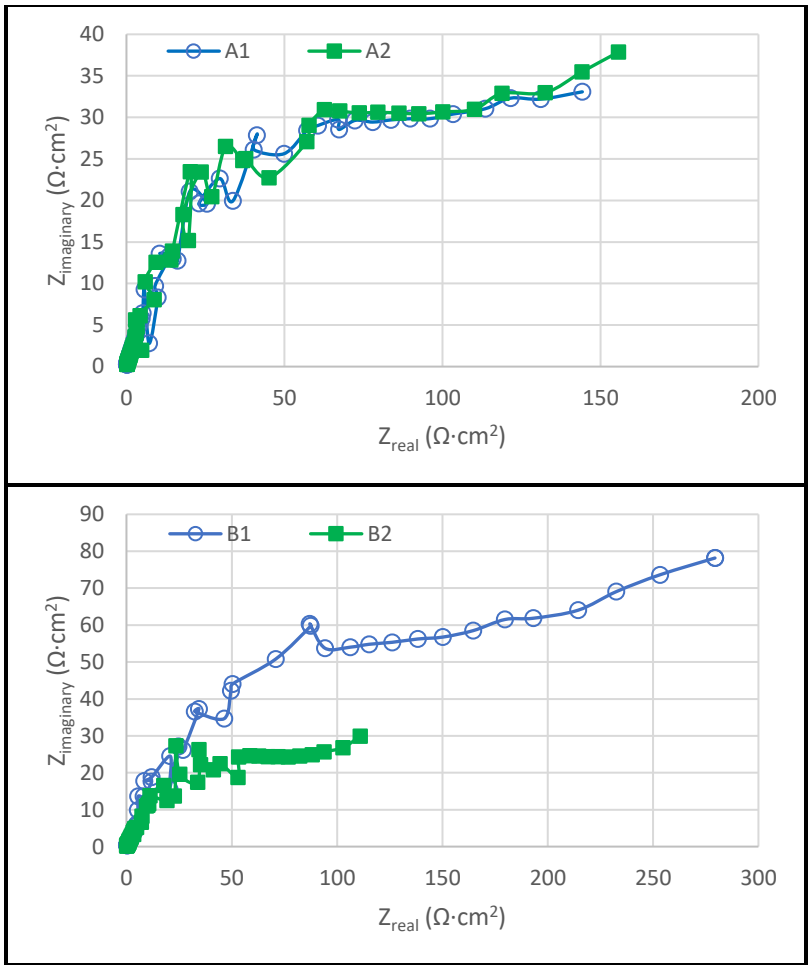

Figure 10. Nyquist plots for Location A (top) and Location B (bottom) at 15% (V/V) H_2SO_4 at 40°

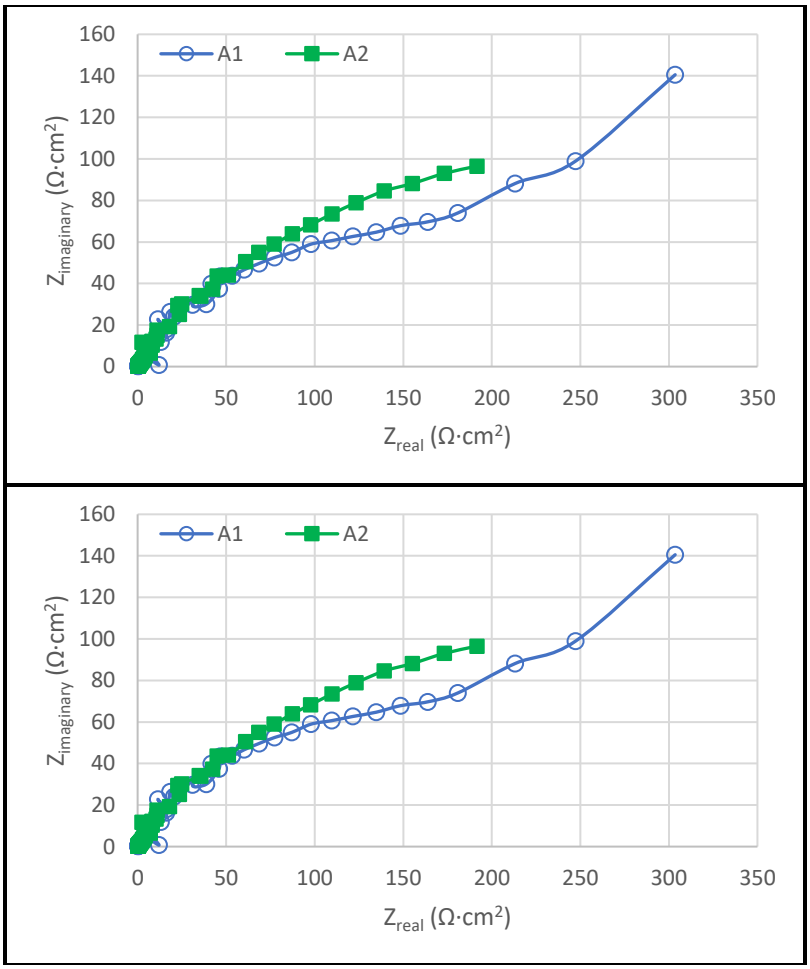

Figure 11. Nyquist plots for Location A (top) and Location B (bottom) at 25% (V/V) H_2SO_4 at 40°C

As mentioned, $PbSO_4$ is formed at the Pb electrode surface when immersed in H_2SO_4 at open circuit potential. The formation of a porous $PbSO_4$ leads to the passivation of the electrode surface [2,10,15]. To better understand the EIS results, an electric circuit model representing the physical elements of the studied electrochemical system was fitted into the Nyquist plots using Z Fit of EC-Lab Software. Figure 12 shows the equivalent circuit representing the physical elements of the electrochemical system. The proposed equivalent circuit was based on the research of Osorio et al. and Li et al. [9,14]. The electrolyte resistance is represented by R_{sol}, the charge transfer resistance on the exposed electrode through the pores is denoted by $R_{CT,}$ and the polarization resistance associated with the porous $PbSO_4$ layer is signified by R_P. The constant phase elements (CPE) representing the capacitance of the double layer and capacitance associated with the polarization resistance are denoted by $Z_{CPE(I)}$ and $Z_{CPE(II),}$ respectively [8,9,14,17–22]. The impedance of a CPE is given by

$$Z_{CPE} = 1 / C(j\omega)^N \quad (1)$$

where C is the capacitance, ω is the frequency, and $-1 \leq N \leq 1$. The physical manifestation of a CPE will be dependent on the value of N. The CPE behaves like a resistor when N = 0, a capacitor when N = 1, an inductor when N = -1, and a Warburg response when N = 0.5 [11], [19]. The CPE was used instead because of the non-ideal capacitive behavior observed from the phase shift angle from the bode plots and the depressed semi-circles of the Nyquist plots.

The goodness of fit was evaluated at a 95% confidence level. The chi-squared value for each model fitting was compared with the critical value of 77.931 derived from the Chi-Square Distribution at a degree of freedom of 59. A good fit is achieved if the chi-squared value is less than 77.931 [23,24]. The chi-squared values for each model fitting are all less than 77.931.

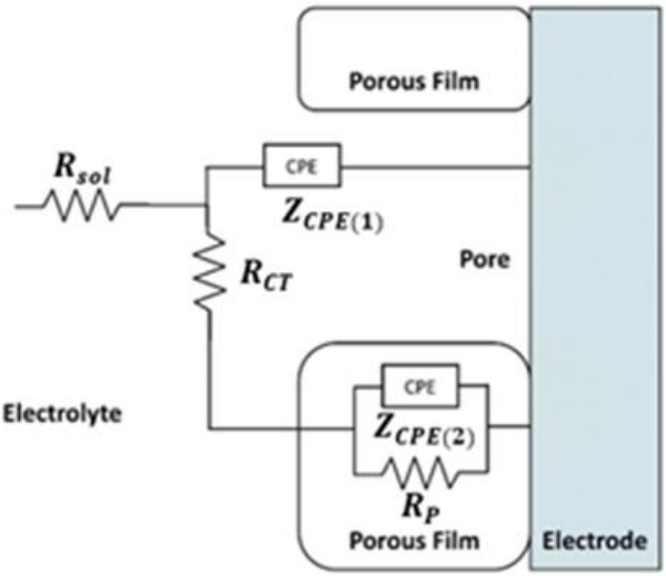

Figure 12. Proposed electrical circuit model [7], [9], [14]

The charge transfer resistance (R_{CT}) values derived from the circuit model fitting are listed in Table 3. Results show that for both locations and acid concentrations, the R_{CT} decreased when the temperature increased as expected of the temperature effect on reaction kinetics. Moreover, the R_{CT} also slightly reduced as the acid concentration increased for both locations at 28°C. The decrease in R_{CT} may be associated with the reduction of active porous sites due to the formation of a more compact $PbSO_4$ layer. The decrease in R_{CT} with the temperature increase was also observed in the study of Osorio et al. [17]. In addition, the R_{CT} in B is also lower than in A at 28°C for both acid concentrations suggesting that the corrosion layer formed in B at 28°C is more compact than in A. On the other hand, the R_{CT} minimally increased as the acid concentration increased for both locations at 40°C.

Table 3. Summary of results of R_{CT} ($\Omega \cdot cm^2$)

Location	Acid Concentration (% V/V)	Temperature (°C)	
		28	40
A	25	11.784	0.510
	15	14.042	0.076
B	25	8.645	3.830
	15	9.430	3.644

The polarization resistance (R_P) values derived from the circuit model fitting are listed in Table 4. Results indicate that the R_P increased with the increase in temperature. The R_P also increased with the increase in acid concentration. The R_P increase may be associated with the formation of a thicker passivating corrosion layer at a higher acid concentration and elevated temperature. The R_P values at location B are higher than in location A indicating the generation of a thicker passivating layer in B than in A. The formation of a thicker passivating layer suggests that corrosion rates are faster in location B. The difference in corrosion tendency and corrosion rates between the grid locations may be attributed to the microstructure difference. Since location B has a finer grain size and cellular size than location A, there are more grain boundary areas and intercellular boundaries. These boundaries are more reactive and susceptible to corrosion than grains because of the higher free energy [17]. The higher values of R_P than R_{CT} indicate that the porous film plays a vital role in the corrosion mechanism [8].

Table 4. Summary of results of R_P ($\Omega \cdot cm^2$)

Location	Acid Concentration (% V/V)	Temperature (°C)	
		28	40
A	25	177.514	335.757
	15	137.038	154.332
B	25	202.095	510.151
	15	129.428	207.607

3.3 Potentiodynamic Polarization Measurements

Polarization curves at 28°C and 40°C are shown in Figures 13 and 14, respectively. Results show that the corrosion potential (E_{CORR}) minimally shifted toward the more negative potential, from -0.993 V to -1.022 V, when the acid concentration increased, indicating that the corrosion tendency marginally increased with H_2SO_4 acid concentration. On the other hand, the E_{CORR} values at different grid locations are comparable. There was also no change in the E_{CORR} when the temperature was increased. Moreover, the polarization curves also exhibit a shift in current density from -0.99V to -1.01V (MSE). Peixoto et al. related this to the formation of $PbSO_4$ [9].

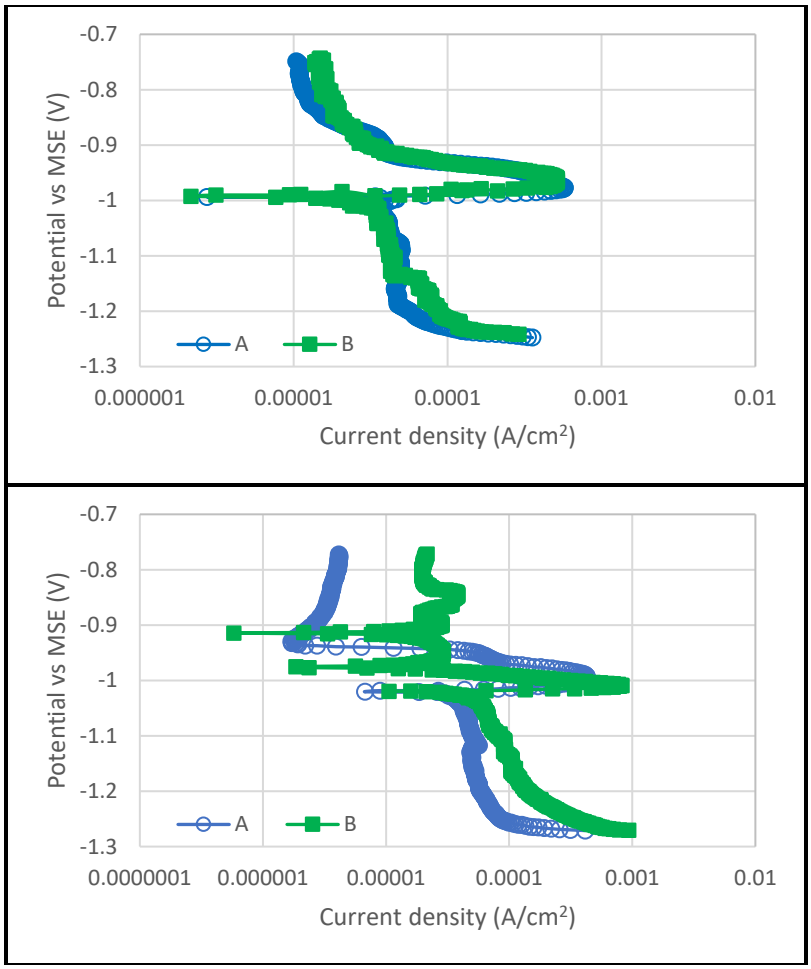

Figure 13. Polarization curves at 15% (V/V) (top) and 25% (V/V) (bottom) H_2SO_4 at 28°C

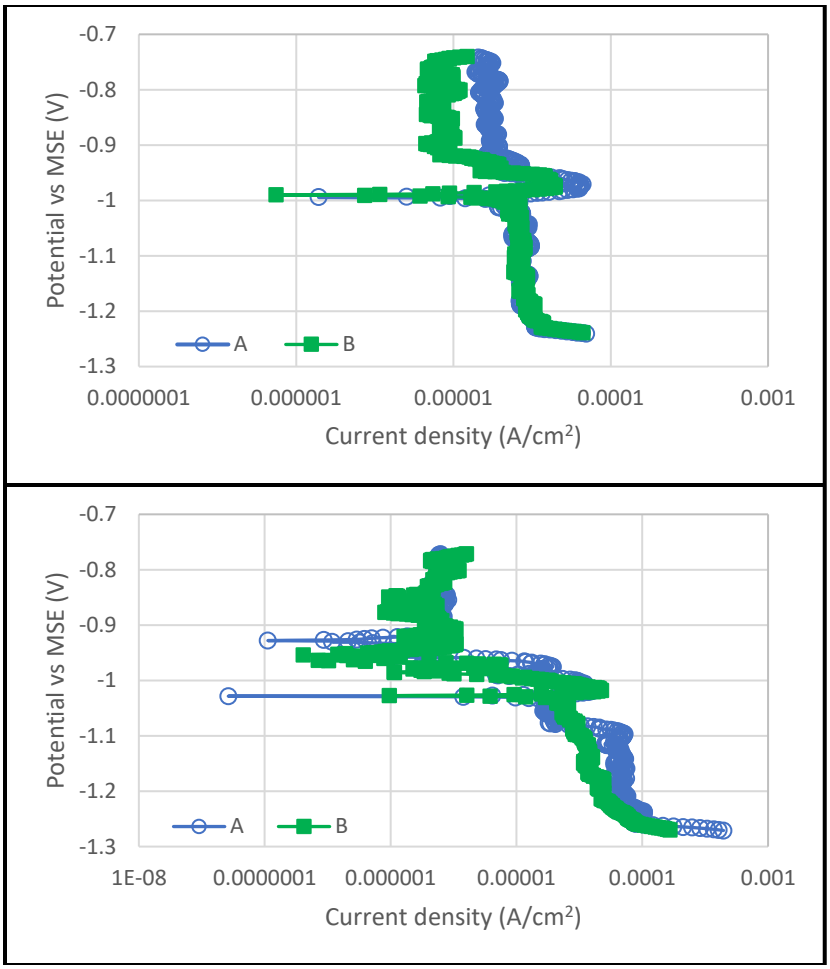

Figure 14. Polarization curves at 15% (V/V) (top) and 25% (V/V) (bottom) H_2SO_4 at 40°C

The polarization resistance (R_P) values derived from the polarization curves are listed in Table 5. Results show that the R_P increased as the temperature increased; this agrees with the established relationship from the EIS results between R_P and temperature. On the other hand, the results also indicate that the effect of increasing the H_2SO_4 concentration on R_P varies between the grid locations.

Table 5. Derived R_P from the polarization curves

Location	H_2SO_4 Concentration (% V/V)	R_P ($\Omega \cdot cm^2$)	
		28°C	40°C
A	25	115.11	402.47
	15	70.56	42.46
B	25	95.66	155.88
	15	199.45	360.31

IV. CONCLUSION AND RECOMMENDATION

Chemical analysis showed that Locations A and B have similar compositions. Photomicrographs show that each grid location is characterized by cellular structures consisting of the Pb-rich α phase with eutectic mixtures on the intercellular boundaries. Location A has a relatively larger grain and cellular size than Location B; this indicates the cooling rate in Location A is slower than in Location B.

EIS was used to evaluate the corrosion behavior of two grid locations at varying acid concentrations and temperatures. The experimental parameters from the curve fitting of the Nyquist plots from the EIS results showed that the charge transfer resistance (R_{CT}) decreased with an increase in working temperature. The decrease in R_{CT} may be associated with the reduction of active porous sites due to the formation of a more compact $PbSO_4$ layer. On the other hand, the R_P increased with the increase in acid temperature and temperature for both grid locations. In addition, The R_P values at location B are higher than in location A. The R_P increase may also be associated with the formation of a thicker passivating corrosion layer which suggests faster corrosion rates. The higher corrosion tendency and corrosion rates in location B may be related to its finer grain and cellular size. As such, manufacturers of as-cast Pb-Ca-Sn grids may consider controlling the cooling rate to produce battery components with better and homogeneous electrochemical behavior.

The polarization curves from the potentiodynamic polarization showed that there was no difference between the E_{CORR} of each grid location. There was also negligible change in the E_{CORR} when the temperature was increased. Results also showed that the R_P derived from the polarization curves increased with the temperature increase; this validates the observed relationship from the EIS results between R_P and temperature.

V. ACKNOWLEDGEMENTS

The authors would like to extend their gratitude to Philippine Batteries Inc. for providing the Pb alloy samples used in the study.

REFERENCES

[1] Prengaman RD. 2001. Challenges from corrosion-resistant grid alloys in lead acid battery manufacturing. J. Power Sources. 95(1–2): 224–233.
[2] Pavlov D. 2017. Lead alloys and grids. Grid Design Principles.
[3] Roma MP. 2010. Electrochemical corrosion of Pb-Ca-Sn alloys. University of the Philippines Diliman.
[4] Zhou YB, Yang CX, Zhou WF, Liu HT. 2004. Comparison of Pb-Sm-Sn and Pb-Ca-Sn alloys for the positive grids in a lead acid battery. J. Alloys Compd. 365(1–2): 108–111.
[5] Hosseini Benhangi P, Nakhaie D, Moayed MH, Molazemi A. 2011. A novel electrochemical approach on the effect of alloying elements on self-discharge and discharge delivered current density of Pb-Ca-Ag lead-acid battery plates. J. Power Sources. 196(23):10424–10429.
[6] Seyedi M, Kosari A, Nakhaie D, Moayed MH, Alagheband A, Azimi MY. 2018. Effect of quenching after solidification on hardness and electrochemical behavior of a Pb-0.09%Ca-1.23%Sn alloy. J. Energy Storage. 17: 441–445.

[7] Osório WR, Peixoto LC, Garcia A. 2009. Electrochemical corrosion of Pb-1 wt% Sn and Pb-2.5 wt% Sn alloys for lead-acid battery applications. J. Power Sources. 194(2): 1120–1127.
[8] Osório WR, Peixoto LC, Garcia A. 2010. Comparison of electrochemical performance of as-cast Pb-1 wt.% Sn and Pb-1 wt.% Sb alloys for lead-acid battery components. J. Power Sources. 195(6):1726–1730.
[9] Peixoto LC, Osório WR, Garcia A. 2009. Microstructure and electrochemical corrosion behavior of a Pb-1 wt%Sn alloy for lead-acid battery components. J. Power Sources. 192(2):724–729.
[10] Peixoto LC, Osório WR, Garcia A. The interrelation between mechanical properties, corrosion resistance and microstructure of Pb-Sn casting alloys for lead-acid battery components. J. Power Sources. 195(2): 621–630.
[11] Mulimbayan F. 2015. Corrosion behavior of austenitic chromium-manganese stainless steels in citric acid. University of the Philippines Diliman.
[12] Gamry Instruments. Retrieved from https://www.gamry.com/application-notes/EIS/basics-of-electrochemical-impedance-spectroscopy/
[13] PalmSens. Retrieved from https://palmsenscorrosion.com/knowledgebase/.
[14] Osório WR, Rosa DM, Garcia A. 2011. Electrolyte features and microstructure affecting the electrochemical performance of a Pb-Sb alloy for lead-acid battery components. Electrochim. Acta. 56(24): 8457–8462.
[15] Pavlov D. 2011. H2SO4 Electrolyte – An Active Material in the Lead–Acid Cell. Elsevier. p. 117–148.
[16] Pavlov D. 2017. Fundamentals of Lead–Acid Batteries. 2nd Ed. Elsevier.
[17] Osório WR, Rosa DM, Garcia A. 2012. Electrochemical behaviour of a Pb-Sb alloy in 0.5M NaCl and 0.5M H_2SO_4 solutions. Mater. Des. 34:660–665.
[18] Wang Y, Li J, Tian Y. 2018. Influence of alloy element addition on the nucleation mechanism of the lead alloy surface and its oxide film properties. J. Alloys Compd. 750:636–643.
[19] Osório WR, Aoki CS C, Garcia A. 2008. Hot corrosion resistance of a Pb-Sb alloy for lead acid battery grids. J. Power Sources. 185(2):1471–1477.
[20] Shervedani RK, Isfahani AZ, Khodavisy R, Hatefi-Mehrjardi A. 2007. Electrochemical investigation of the anodic corrosion of Pb-Ca-Sn-Li grid alloy in H2SO4 solution. J. Power Sources. 164(2):890–895.
[21] Burashnikova MM, Zotova IV, Kazarinov IA. 2013. Pb-Ca-Sn-Ba grid alloys for valve-regulated lead acid batteries. Engineering. 5:9–15.
[22] Earths MN. 2006. Effect of cerium on gas evolution behavior of Pb-Ca-Sn alloy. J. Rare Earths. 24(2):2–7.
[23] Montgomery D. Runger G. 2011. Applied statistics and probability for engineers. 5th ed. New Jersey:Wiley.
[24] National Insitute of Standards and Technology. Retrieved from https://www.itl.nist.gov/div898/handbook/eda/section3/eda3674.htm.